Giant spin splitting of the two-dimensional electron gas at the surface of SrTiO$_3$

A. F. Santander-Syro,[1, *] F. Fortuna,[1] C. Bareille,[1] T. C. Rödel,[1]

G. Landolt,[2, 3] N. C. Plumb,[3] J. H. Dil,[2, 3, 4, †] and M. Radović[3, 5, ‡]

[1]*CSNSM, Université Paris-Sud and CNRS/IN2P3,*

Bâtiments 104 et 108, 91405 Orsay cedex, France

[2]*Physik-Institut, Universität Zürich,*

Winterthurerstrasse 190, 8057 Zürich, Switzerland

[3]*Swiss Light Source, Paul Scherrer Institut, CH-5232 Villigen PSI, Switzerland*

[4]*Institute of Condensed Matter Physics,*

Ecole Polytechnique Fédérale de Lausanne, CH-1015 Lausanne, Switzerland

[5]*SwissFEL, Paul Scherrer Institut, CH-5232 Villigen PSI, Switzerland*

1

Two-dimensional electron gases (2DEGs) forming at the interfaces of transition metal oxides [1–3] display a range of properties including tunable insulator-superconductor-metal transitions [4–6], large magnetoresistance [7], coexisting ferromagnetism and superconductivity [8, 9], and a spin splitting of a few meV [10, 11]. Strontium titanate ($SrTiO_3$), the cornerstone of such oxide-based electronics, is a transparent, nonmagnetic, wide-band-gap insulator in the bulk, and has recently been found to host a surface 2DEG [12–15]. The most strongly confined carriers within this 2DEG comprise two sub-bands, separated by an energy gap of 90 meV and forming concentric circular Fermi surfaces [12, 13, 15]. Using spin- and angle-resolved photoemission spectroscopy (SARPES), we show that the electron spins in these sub-bands have opposite chiralities. Although the Rashba effect might be expected to give rise to such spin textures, the giant splitting of almost 100 meV at the Fermi level is far larger than anticipated [16, 17]. Moreover, in contrast to a simple Rashba system, the spin-polarized sub-bands are non-degenerate at the Brillouin zone centre. This degeneracy can be lifted by time-reversal symmetry breaking, implying the possible existence of magnetic order. These results show that confined electronic states at oxide surfaces can be endowed with novel, non-trivial properties that are both theoretically challenging to anticipate and promising for technological applications.

The 2DEG at the surface of $SrTiO_3$, formed by confined electrons of the t_{2g} conduction band with Ti-3d character, is universal in the sense that its constituent subbands, their fillings, and their Fermi surfaces are independent of the bulk sample doping and of whether the surfaces are prepared by cleaving [12, 13] or by etching and *in situ* annealing [15]. This 2DEG consists on two light electron subbands dispersing down to about -180 meV and, respectively, -90 meV below the Fermi level (E_F), producing concentric Fermi surfaces around the Brillouin zone center, and heavy shallow subbands dispersing down to about -40 meV, forming ellipsoidal Fermi surfaces [12, 13, 15].

In fact, the 2DEG in $SrTiO_3$ has been associated with a band-bending of ~ 300 meV at the surface of the material [12, 13, 15]. In such a quantum well profile, the most bound light subbands are tightly confined near the surface, while the less bound heavy subbands are more delocalized towards the bulk [12, 15]. The present work focuses on resolving the spin

structure of the strongly two-dimensional light subbands, which are the most technologically relevant in terms of their carrier concentration and mobility.

The surface band-bending of ~ 300 meV amounts to an electric field $\mathcal{F} \sim 100$ MV/m confining the conduction electrons near the surface. In a simple approximation, this field will induce a so-called "Rashba splitting" of the spin states in each subband, with the largest splitting occurring for the most bound subbands. In an ideal surface, the corresponding momentum separation (k_R) will be of the order of $k_R \approx 2e\mathcal{F}/\Delta$, where Δ is the gap between the valence and conduction bands [14, 18]. For $\mathcal{F} \sim 100$ MV/m and $\Delta \sim 3.5$ eV, typical of the 2DEG at the surface of SrTiO$_3$[12, 15], the momentum spin splitting at E_F is thus expected to be of the order of $k_R \sim 6 \times 10^{-3}$ Å^{-1}, at the limit of the best resolutions today available in ARPES. For the light subbands in SrTiO$_3$, such momentum splitting amounts to an energy splitting of a few meV near E_F, as indeed inferred from magneto-transport measurements in the 2DEG at LaAlO$_3$/SrTiO$_3$ interfaces subject to a strong voltage bias [10, 11], and also predicted by *ab initio* calculations of the 2DEG at such interfaces [16, 17]. However, the possible spin splitting of the 2DEG at the surface of SrTiO$_3$ has not been measured so far.

As we will see next, in marked contrast to the above expectations, our data reveal an astounding discovery: first, *each* of the light subbands of the 2DEG at the surface of SrTiO$_3$ is spin polarized, with spins winding in helical texture around the Fermi surface, such that the momentum spin splitting is one order of magnitude larger than the one estimated above, and second, the electronic structure is gapped at $\vec{k} = 0$, which is not expected in a simple Rashba picture.

For our experiments, we prepared *in situ* the 2DEG on (001)-oriented TiO$_2$ terminated surfaces of SrTiO$_3$ [15] (Methods). This produces pristine mono-crystalline surfaces showing a 2DEG with light and heavy subbands (Supplementary Note 1), identical to the ones observed in cleaved SrTiO$_3$ surfaces [12, 13], but with much sharper photoemission lines and a larger signal-to-background ratio, which are crucial for SARPES measurements. For reasons explained earlier, we focus henceforth on the two lowest light subbands. To this end, we take advantage of the fact that the photoemission signal from the heavy subbands can be "silenced" by dipole-transition selection rules, through a combination of experimental geometry and light energy and polarization, leaving only the light subbands, as fully documented in Ref.[12] (see also Supplementary Note 1).

The geometry of the experimental setup is schematically shown in Fig. 1(a). Figure 1(b) shows the circular Fermi surfaces of the 2DEG, measured in spin-integrated mode with the channeltron detectors of the SARPES setup. These Fermi surfaces are generated by two light parabolic subbands, whose dispersions along the (010) and (100) directions in reciprocal space are shown by the colour plots in Figs. 1(e, h).

We now discuss our spin-resolved measurements near the Fermi level (E_F). Figure 1(c) shows the populations of electrons with momentum along (010) having their spin parallel (up) or anti-parallel (down) to the local, *i.e.*, momentum-dependent, spin quantization axis $\vec{Q}$ (determined below and further discussed in the Supplementary Note 2). Figure 1(d) shows the resulting spin polarization along $\vec{Q}$ as a function of electron momentum along (010). Figures 1(f, g) show the corresponding spin-resolved data for electron momentum along the (100) direction.

The data in Fig. 1 demonstrates that the two light subbands are *spin polarized*, with each band showing *opposite spin orientations at opposite Fermi momenta* –in other words, there is a spin-momentum locking causing a non-trivial spin texture. Indeed, the momentum separation at E_F between opposite spin states, given directly by the data in Figs. 1(c, f), is equal to the difference in Fermi momenta between the two subbands, namely about 0.1 Å^{-1}.

To further understand the spin-resolved data and determine $\vec{Q}$, we analyzed the momentum distribution curves (MDCs) at different binding energies. Thus, we fitted simultaneously the total spin-integrated MDC and the spin-polarizations along the local x (tangential to the Fermi surface), y (radial) and z (out-of-plane) axes using a well established quantitative vectorial analysis routine [19]. For definiteness, we concentrate on the subband dispersions along the (010) direction. These are shown again, for clarity in the discussion, in the colour plots of Figs. 2(a, f, k). For measurements at the Fermi level, presented in Figs. 2(a–d), the results of such fits are plotted as orange lines on top of the symbols showing the spin-integrated [Fig. 2(a)] and spin-resolved [Figs. 2(b–d)] data. From these measurements and fits, it can be concluded that *each light sub-band is spin-polarized at the Fermi level*, and that *the spin vectors wind tangentially to the Fermi contours*, with only a small out-of-plane component. Figure 2(e) shows the projection along x of the 3D spin-polarization vectors around E_F, obtained from the above data analysis. The amplitude of each spin-polarization vector, given by the fits, is $|P_{fit}| = 1$. This means that the detected free electrons photo-emitted from the surface, whose spin polarization is well defined, have all spins essentially oriented

along the same direction, tangential to the Fermi surface. These measured spin-splitting and polarizations are robust with respect to changes in photon energy and polarization (see below and Supplementary Note 3), supporting the interpretation as an intrinsic spin structure of the light subbands [20].

Figs. 2(f-i) show the analysis of the spin-integrated and spin-resolved data taken around $E = -130$ meV. In this case, we find a reduced measured polarization vector length (40%) for the inner band, and a fully polarized (100%) outer band, as summarized in Fig. 2(j). Likewise, the fits to data taken in the gap between the two bands at $E = -190$ meV, presented in Figs. 2(k–n), demonstrate that the degree of measured polarization of the outer subband decreases to 80% when approaching the band minimum, as seen from the corresponding spin vectors plotted in Fig. 2(o). Thus, at this latter energy, a cut through the entire surface Brillouin zone consists of only a single spin-polarized contour.

Now, a *crucial* difference between the spin-split electronic structure measured here for the SrTiO$_3$ surface and a typical Rashba system is the absence, in our case, of a band crossing at $\vec{k} = 0$ [12, 13, 15] –see for instance the experimental band dispersions in Fig. 1(c) and Fig. 2(a). Note that, under time-reversal symmetry, electron eigenstates $E(\vec{k}, \uparrow)$ of energy E, momentum $\vec{k}$ and spin $\uparrow$, transform into $E(-\vec{k}, \downarrow)$, meaning that for $\vec{k} = 0$ the bands should be degenerate. The absence of this Dirac point in our data points to a further unique property of the SrTiO$_3$ surface, namely *the co-existence of a spin splitting of helical texture and some form of magnetism.* Indeed, an out-of-plane component of an intrinsic magnetic moment can lift the above degeneracy and open up an additional gap for all momenta, including around $\vec{k} = 0$ [21]. Note also that our experiments were done in zero external magnetic field, to conserve the electron wave-vector, essential for momentum-resolved measurements.

Thus, the combination of helical spin texture and magnetism with a sizeable component along the z-direction should lead to the occurrence of an out-of-plane spin-polarization P_z of increasing amplitude close to the bottom of the band, as observed for topological insulators [22]. However, in the absence of an external magnetic field, both magnetic orientations along the z-axis are equally probable, and P_z will average to zero in macroscopic measurements such as SARPES. The total spin, however, is conserved and any canting of the spin along $\pm z$, implying the occurrence of domains with spin polarizations $\pm P_z$ in that direction, will result in a reduced component of the measured in-plane spin polarization. This is indeed compatible with the binding-energy-dependent SARPES measurements discussed in Fig. 2.

Therefore, all the data of Fig. 2 show that the spin polarization and winding on each subband are maintained down to the lowest binding energies. Note in particular that the spin texture of the outer subband keeps a large in-plane polarization amplitude even in the gap between the two subbands, from about $E = -130$ meV to $E = -190$ meV. This suggests that the mechanism responsible for the helical in-plane spin texture is the main energy scale at large momenta. This energy scale is then one order of magnitude larger than both the one so far reported in LaAlO$_3$/SrTiO$_3$ interfaces [10, 11], and the one expected from a naive Rashba model that takes solely into account the confining electric field. Such a strong deviation from the original Rashba scenario has been *demonstrated* for model metallic systems by numerous previous works [23, 24], and is attributed as a general property of the surface corrugation and the associated wave-function asymmetry [23–26], which results in a greatly enhanced Rashba parameter that increases the spin splitting. Thus, the large spin splitting of helical spin texture observed in our data may signal the relevance of surface corrugations for understanding the electronic and spin structure of the 2DEG at the surface of SrTiO$_3$.

Figure 3 is a schematic summary of our findings for the electronic structure of the light subbands at the surface of SrTiO$_3$. As shown by the illustration in Fig. 3(a), these light subbands can be depicted in terms of coexisting Rashba and Zeeman splittings, with the first dominating at large momenta, and the second dominating around $\vec{k} = 0$. In Fig. 3(a), the sombrero-like form of the bottom of the lower band has been largely exaggerated: even for Rashba splittings comparable to the magnetic splitting at $\vec{k} = 0$, one would obtain two almost parabolic bands (Supplementary Note 4). We stress thus that Fig. 3(a) is an *oversimplified image*, whereas our results and conclusions are dictated solely by the data, and are independent of any theoretical model or analysis.

To facilitate the remaining discussion, we label from 1 to 4 each of the subband branches, as shown in Fig. 3(a). We also introduce, in Fig. 3(b), the local $\{xyz\}$ axes and a schematic polar representation of the 3D spin vectors. Thus, we show in Figs. 3(c–f) the 3D spin vectors at E_F for the light subbands of the 2DEG at the surface of SrTiO$_3$, obtained from 4 different sets of measurements at various photon energies and polarizations. Data and fits corresponding to these measurements are presented in the Supplementary Note 3.

As seen from Figs. 3(c–f), all the different measurements give consistent polarization vectors, although all sets were fitted independently. Note in particular that, for each of

the subband branches, P_x is compatible between all the data sets, which furthermore show systematically the opposite non-trivial spin-winding textures for the inner and outer light bands. These results prove that the helical spin structure, the giant spin splitting, and the subband spin polarization reported in this work, are all independent of the photon energy and polarization, hence inherent to the electronic structure of the 2DEG at the surface of $SrTiO_3$ [20]. On the other hand, contrary to P_x, which does not change with photon energy or polarization, the out-of-plane component (P_z) of the spin polarization for the inner subband presents an anomaly (it gets inverted) at $h\nu = 52$ eV. This suggests that P_z originates from extrinsic matrix elements of the SARPES process (Supplementary Note 3).

The possibility that the two light subbands of the 2DEG in $SrTiO_3$ are oppositely spin polarized had been overlooked in previous works [12, 13, 15], mainly for two reasons mentioned earlier. First, the splitting of the spin polarized state, namely ~ 0.1 Å^{-1}, or about 100 meV at E_F, is unexpectedly large. Second, and perhaps even more surprisingly, the nondegenerate state of these two subbands at the Brillouin zone center is not expected in a pure Rashba scenario, and implies the existence of a heretofore unobserved magnetic order associated with the metallic surface. In fact, while these two light subbands show very different photoemission selection rules upon illumination with orthogonal photon polarizations, suggesting that they originate from orthogonal $3d$ orbitals [12], the Fermi surfaces they generate are both perfectly circular, indicating that they have the same d_{xy} orbital character [13, 15]. These apparently contradictory observations of previous works can be reconciled by considering one crucial element –spin– that had been overlooked up to now: note that the *total* symmetry of each confined state is given by both the orbital and spinor parts of its wave function. Thus, our data demonstrates that the two light subbands at the surface of $SrTiO_3$ correspond to two d_{xy}-like bands, but with the *spins* of the electrons in each band locked to their momenta in *opposite* winding patterns. In other words, these subbands differ fundamentally in the symmetry of their *total spin-orbital* wavefunctions.

Our data are the first, direct demonstration of a non-trivial spin texture showing both a giant spin-splitting and magnetism in the 2DEG at the bare surface of $SrTiO_3$ or any other oxide. In the case of $SrTiO_3$-based heterostructures, where ferromagnetism has been previously reported [7–9], recent X-ray magnetic circular dichroism experiments found it to arise from d_{xy} orbitals of Ti^{3+} character [27], and to be quenched by annealing in oxygen, suggesting a decisive role of oxygen vacancies in this phenomenon [28]. Interestingly, the-

oretical calculations have found that clusters of oxygen vacancies could induce an orbital reconstruction, generating an interfacial magnetic state with a dominant contribution from the d_{xy} states to the magnetic moment and an exchange energy splitting as large as a fraction of eV [29, 30]. Alternative models, based the interfacial splitting of t_{2g} orbital degeneracy in combination with electron correlations, have also been proposed [2, 31–34].

It is interesting to contrast our findings with the case of spin-polarized quantum well states in ultra-thin films of non-magnetic materials grown on ferromagnetic surfaces, like *e.g.* Cu/Co(001) [35, 36]. In the latter case, the spin polarization of the bands in the non-magnetic overlayer is induced by their interaction with the magnetic states in the substrate [35, 36], and is of trivial ferromagnetic type, *i.e.*, the spin vectors are parallel for opposite momenta. In the case of SrTiO$_3$, on the other hand, the *bulk* material is merely a transparent paramagnetic band insulator at all temperatures, while the 2DEG at its surface shows both a *non-trivial* helical spin texture and magnetism. These original spin-polarized states must then clearly arise from intrinsic properties of the 2DEG and the spatial region where it is confined.

Thus, in analogy with the case of magnetism in SrTiO$_3$-based heterostructures, we speculate that for the 2DEG at the bare SrTiO$_3$ surface not only the surface-induced translational-symmetry breaking and subband orbital ordering [12], but also oxygen vacancies [12, 13], and possibly lattice distortions [37] and/or electron exchange correlations, may play a fundamental role in establishing the observed non-trivial magnetic ground state. The exploration of all these possibilities, and the microscopic explanation of our observations, are at this point open issues beyond the scope of this work, and should be the subject of future theoretical and experimental research.

In a broader perspective, the spin structure unveiled by our data has far reaching consequences both for applications and for fundamental physics. SrTiO$_3$ represents the first example of a system with a large spin-splitting at the Fermi level, 4 times larger than room temperature, located on a truly insulating substrate. This opens promising avenues for the realization of oxide-based spintronic devices. Additionally, an exciting possibility would be tuning the Fermi level, for instance by chemical doping of the surface or by field effect, to lie exactly within the gap between the two spin-polarized subbands, yielding a single Fermi contour where the spin orientations are locked to the momenta. Such a spin structure, in conjunction with superconductivity, which occurs below 250 mK in SrTiO$_3$ [38] and

8

LaAlO$_3$/SrTiO$_3$ heterostructures [5] for certain doping regime, are the key ingredients for achieving the hotly-pursued Majorana fermion. Such a scenario would be the 2D analog of 1D InSb nano-wires, where Majorana-like point modes were observed in proximity to a superconductor [39]. Given the rich phase diagrams of complex metallic oxides, and the spin structure observed here on SrTiO$_3$, oxide surface states now emerge as promising systems towards new physics and functionalities.

METHODS

To realize TiO$_2$-terminated surfaces, the (001)-oriented SrTiO$_3$ crystals (SurfaceNet GmbH) were etched in an HF solution, and then annealed *ex-situ* at 1000°C in a flow of oxygen during 1 hour. The samples were then transferred to an UHV chamber, and re-annealed in an oxygen atmosphere of 100 mbar at 500°C for one hour. The surface quality was simultaneously monitored by reflection high energy electron diffraction (RHEED), showing clearly the 1×1 diffraction pattern of the SrTiO$_3$-(001) surface. This treatment was followed by a second UHV annealing (10^{-10} mbar) at $250 - 300$°C. The whole procedure yields transparent samples with conducting surfaces, as confirmed by the absence of charging effects in low energy electron diffraction (LEED), STM and ARPES measurements *(15)*. The samples were finally transferred to the SARPES station without breaking the UHV.

The SARPES experiments were done at the COPHEE end-station of the SIS beamline [40], Swiss Light Source (SLS), using linearly- and circular-polarized photons in the energy range 30-80 eV, and an Omicron EA 125 hemispherical energy analyzer equipped with two orthogonally mounted classic Mott detectors. These detectors, based on the spin-orbit scattering of the incident electron beam off a gold target, allow measuring the electron spin without using an applied magnetic field, which would otherwise affect the momentum vector of the outgoing photoelectrons. The whole setup allows for the simultaneous measurements of all three spatial components of the spin polarization vector for each point of the band structure. In this work, we concentrated on measuring spin-resolved MDCs, as they allow a direct, immediate visualization of both the spin splitting at different momenta and the spin texture around different Fermi surfaces. The angular and energy resolutions in spin-resolved mode were 1.5° and 60 meV, respectively. In spin-integrated mode the resolutions where set to 0.5° and 20 meV. The incident photon beam was smaller than $200 \times 200 \mu$m

and $200 \times 800\mu$m for the spin integrated and spin resolved measurements respectively. All data was taken at $T = 20$ K. The results were reproduced on 4 samples over 3 different experimental runs.

ACKNOWLEDGEMENTS

AUTHOR CONTRIBUTIONS

Project conception: A.F.S.-S., F.F., J.H.D, M.R.; measurements: A.F.S.-S., F.F., C.B., T.R., G.L., N.C.P., J.H.D., M.R.; infrastructure for SARPES experiments at SLS: G.L., J.H.D; sample characterizations: N.C.P, M.R; data analysis: A.F.S.-S, F.F., J.H.D.; writing of the manuscript: A.F.S.-S., F.F., J.H.D. All authors discussed extensively the results and the manuscript.

COMPETING INTERESTS

The authors declare that they have no competing financial interests.

ADDITIONAL INFORMATION

Correspondence and requests for materials should be addressed to A.F.S.S. (andres.santander@csnsm.in2p3.fr), J.-H.D (hugo.dil@epfl.ch), and M.R. (milan.radovic@psi.ch).

* andres.santander@csnsm.in2p3.fr

† hugo.dil@epfl.ch

‡ milan.radovic@psi.ch

[1] Ohtomo, A., and Hwang, H. Y. A high-mobility electron gas at the $LaAlO_3/SrTiO_3$ heterointerface. *Nature* **427,** 423-426 (2004).

[2] Okamoto, S., and Millis, A. J. Electronic reconstruction at an interface between a Mott insulator and a band insulator. *Nature* **428,** 630 (2004).

[3] Hwang, H. Y, Iwasa, Y., Kawasaki, M., Keimer, B., Nagaosa, N., and Tokura, Y. Emergent phenomena at oxide interfaces. *Nature Mater.* **11,** 103-113 (2012).

[4] Thiel, S., Hammerl, G., Schmehl, A., Schneider, C. W., and Mannhart, J. Tunable quasi-two-dimensional electron gases in oxide heterostructures. *Science* **313,** 1942-1945 (2006).

[5] Reyren, N., Thiel, S., Caviglia, A. D., Fitting Kourkoutis, L., Hammerl, G., Richter, C., Schneider, C. W., Kopp, T., Rüetschi, A.-S., Jaccard, D., Gabay, M., Muller, D. A., Triscone, J.-M., and Mannhart, J. Superconducting interfaces between insulating oxides. *Science* **317,** 1196-1199 (2007).

[6] Ueno, K., Nakamura, S., Shimotani, H., Ohtomo, A., Kimura, N., Nojima, T., Aoki, H., Iwasa, Y., and Kawasaki, M. Electric-field-induced superconductivity in an insulator. *Nature Mater.* **7,** 855-858 (2008).

[7] Brinkman, A., Huijben, M., van Zalk, M., Huijben, J., Zeitler, U., Maan, J. C., van der Wiel, W. G., Rijnders, G., Blank, D. H. A., and Hilgenkamp, H. Magnetic effects at the interface between non-magnetic oxides. *Nature Mater.* **6,** 493-496 (2007).

[8] Li, L., Richter, C., Mannhart, J., and Ashoori, R. C.. Coexistence of magnetic order and two-dimensional superconductivity at $LaAlO_3/SrTiO_3$ interfaces. *Nature Phys.* **7,** 762-766 (2011).

[9] Bert, J. A., Kalisky, B., Bell, C., Kim, M., Hikita, Y., Hwang, H. Y., and Moler, K. A. Direct imaging of the coexistence of ferromagnetism and superconductivity at the $LaAlO_3/SrTiO_3$ interface. *Nature Phys.* **7,** 767-771 (2011).

[10] Caviglia, A. D., Gabay, M., Gariglio, S., Reyren, N., Cancellieri, C., and Triscone, J.-M. Tunable Rashba spin-orbit interaction at oxide interfaces. *Phys. Rev. Lett.* **104,** 126803 (2010).

[11] Ben Shalom, M., Ron, A., Palevski, A., and Dagan, Y. Shubnikov-De Haas oscillations in SrTiO$_3$/LaAlO$_3$ interfaces. *Phys. Rev. Lett.* **105,** 206401 (2010).

[12] Santander-Syro, A. F., Copie, O., Kondo, T., Fortuna, F., Pailhès, S., Weht, R., Qiu, X. G, Bertran, F., Nicolaou, A., Taleb-Ibrahimi, A., Le Fèvre, P., Herranz, G., Bibes, M., Reyren, N., Apertet, Y., Lecoeur, P., Barthélémy, A., and Rozenberg, M. J. Two-dimensional electron gas with universal subbands at the surface of SrTiO$_3$. *Nature* **469,** 189-193 (2011).

[13] Meevasana, W., King, P. D. C., He, R. H., Mo, S.-K, Hashimoto, M., Tamai, A., Songsiriritthigul, P., Baumberger, F., and Shen, Z.-X. Creation and control of a two-dimensional electron liquid at the bare SrTiO$_3$ surface. *Nature Mater.* **10,** 114-118 (2011).

[14] Santander-Syro, A. F., Bareille, C., Fortuna, F., Copie, O., Gabay, M., Bertran, F., Taleb-Ibrahimi, A., Le Fèvre, P., Herranz, G., Reyren, N., Bibes, M., Barthélémy, A., Lecoeur, P., Guevara, J., and Rozenberg, M. J. Orbital symmetry reconstruction and strong mass renormalization in the two-dimensional electron gas at the surface of KTaO$_3$. *Phys. Rev. B* **86,** 121107 (2012).

[15] Plumb, N. C., Salluzzo, M., Razzoli, E., Månsson, M., Falub, M., Krempasky, J., Matt, C. E., Chang, J., Schulte, M., Braun, J., Ebert, H., Minár, J., Delley, B., Zhou, K.-J., Schmitt, T., Shi, M., Mesot, J., Patthey, L., and Radović, M. Mixed dimensionality of confined conducting electrons in the surface region of SrTiO$_3$. *Phys. Rev. Lett.* **113,** 086801 (2014).

[16] Khalsa, G. Lee, B., and MacDonald, A. H. Theory of t_{2g} electron-gas Rashba interactions. *Phys. Rev. B* **88,** 041302(R) (2013).

[17] Zhong, Z., Zhang, Q., and Held, K. Quantum confinement in perovskite oxide heterostructures: Tight binding instead of a nearly free electron picture. *Phys. Rev. B* **88,** 125401 (2013).

[18] Winkler, R. *Spin-Orbit Coupling Effects in Two-Dimensional Electron and Hole Systems.* (Springer, Berlin, 2003).

[19] Meier, F., Dil, J. H., and Osterwalder, J. Measuring spin polarization vectors in angle-resolved photoemission spectroscopy. *New J. Phys.* **11,** 125008 (2009).

[20] Osterwalder, J. Can spin-polarized photoemission measure spin properties in condensed matter? *J. Phys.: Condens. Matter* **24,** 171001 (2012).

[21] Potter, A. C., and Lee, P. A. Multichannel generalization of Kitaev's Majorana end states and a practical route to realize them in thin-films. *Phys. Rev. Lett.* **105,** 227003 (2010).

[22] Xu, S.-Y., Neupane, M., Liu, C., Zhang, D., Richardella, A., Wray, L. A., Alidoust, N., Leandersson, M., Balasubramanian, T., Sanchez-Barriga, J., Rader, O., Landolt, G., Slomski, B., Dil, J. H., Osterwalder, J., Chang, T.-R., Jeng, H.-T., Lin, H., Bansil, A., Samarth, N., and Hasan, M. Z. Hedgehog spin texture and Berry's phase tuning in a magnetic topological insulator. *Nature Phys.* **8,** 616-622 (2012).

[23] Dil, J. H. Spin and angle resolved photoemission on non-magnetic low-dimensional systems. *J. Phys.: Condens. Matter* **21,** 403001 (2009).

[24] Gierz, I., Stadtüller, B., Vuorinen, J., Lindroos, M., Meier, F., Dil, J. H., Kern, K., and Ast, C. R. Structural influence on the Rashba-type spin splitting in surface alloys. *Phys. Rev. B* **81,** 245430 (2010).

[25] Bihlmayer, G., Koroteev, Yu. M., Echenique, P. M., Chulkov, E. V., and Blügel, S. The Rashba effect at metallic surfaces. *Surface Science* **600,** 3888-3891 (2006).

[26] Nagano, M., Kodama, A., Shishidou, T., and Oguchi, T. A first-principles study on the Rashba effect in surface systems. *J. Phys.: Condens. Matter* **21,** 064239 (2009).

[27] Lee, J.-S., Xie, Y. W., Sato, H. K., Bell, C., Hikita, Y., Hwang, H. Y., and Kao, C.-C. Titanium d_{xy} ferromagnetism at the LaAlO$_3$/SrTiO$_3$ interface. *Nature Mater.* **12,** 703-706 (2013).

[28] Salluzzo, M., Gariglio, S., Stornaiuolo, D., Sessi, V., Rusponi, S., Piamonteze, C., De Luca, G. M., Minola, M., Marré, D, Gadaleta, A., Brune, H., Nolting, F., Brookes, N. B., and Ghiringhelli, G. Origin of interface magnetism in BiMnO$_3$/SrTiO$_3$ and LaAlO$_3$/SrTiO$_3$ heterostructures. *Phys. Rev. Lett.* **111,** 087204 (2013).

[29] Pavlenko, N., Kopp, T., Tsymbal, E. Y., Mannhart, J., and Sawatzky, G. A. Oxygen vacancies at titanate interfaces: Two-dimensional magnetism and orbital reconstruction. *Phys. Rev. B* **86,** 064431 (2012).

[30] Pavlenko, N., Kopp, T., Tsymbal E. Y., Sawatzky, G. A., and Mannhart, J. Magnetic and superconducting phases at the LaAlO$_3$/SrTiO$_3$ interface: The role of interfacial Ti $3d$ electrons. *Phys. Rev. B* **85,** 020407(R) (2012).

[31] Michaeli, K., Potter, A. C., and Lee, P. A. Superconducting and ferromagnetic phases in SrTiO$_3$/LaAlO$_3$ oxide interface structures: Possibility of finite momentum pairing. *Phys. Rev. Lett.* **108,** 117003 (2012).

13

[32] Banerjee, S., Erten, O., and Randeria, M. Ferromagnetic exchange, spin-orbit coupling and spiral magnetism at the LaAlO$_3$/SrTiO$_3$ interface. *Nature Phys.* **9,** 626-630 (2013).

[33] Okamoto, S., Millis, A. J., and Spaldin, N. A. Lattice relaxation in oxide heterostructures: LaTiO$_3$/SrTiO$_3$ superlattices. *Phys. Rev. Lett.* **97,** 056802 (2006).

[34] Pentcheva, R., and Pickett, W. E. Ionic relaxation contribution to the electronic reconstruction at the n-type LaAlO$_3$/SrTiO$_3$ interface. *Phys. Rev. B* **78,** 205106 (2008).

[35] Garrison, K., Chang, Y., and Johnson, P. D. Spin polarization of quantum well states in copper thin films deposited on a Co(001) substrate. *Phys. Rev. Lett.* **71,** 2801-2804 (1993).

[36] Carbone, C., Vescovo, E., Rader, O., Gudat, W., and Eberhardt, W. Exchange split quantum well states of a noble metal film on a magnetic substrate. *Phys. Rev. Lett.* **71,** 2805-2808 (1993).

[37] Bickel, N., Schmidt, G., Heinz, K., and Müller, K. Ferroelectric relaxation of the SrTiO$_3$(100) surface. *Phys. Rev. Lett.* **62,** 2009-2011 (1989).

[38] Schooley, J. F., Hosler, W. R., and Cohen, M. L. Superconductivity in semiconducting SrTiO$_3$. *Phys. Rev. Lett.* **12,** 474-475 (1964).

[39] Mourik, V., Zuo, K., Frolov, S. M., Plissard, S. R., Bakkers, E. P. A. M., and Kouwenhoven, L. P. Signatures of Majorana fermions in hybrid superconductor-semiconductor nanowire devices. *Science* **336,** 1003-1007 (2012).

[40] Hoesch, M., Greber, T., Petrov, V. N., Muntwiler, M., Hengsberger, M., Auwärter, W., and Osterwalder, J. Spin-polarized Fermi surface mapping. *J. Electron Spectrosc. Relat. Phenom.* **124,** 263-279 (2002).

FIG. 1. **Spin polarized subbands of the 2DEG at the surface of SrTiO$_3$.** (**a**) Schematic experimental geometry. The incident light beam (energy $h\nu$) and the outgoing electrons entering the detector define the scattering plane, horizontal in this case. Light polarization (horizontal or vertical) is referred to this plane. Reciprocal space along (100) and (010) is explored by varying, respectively, the angles θ and ψ. (**b**) ARPES Fermi surface map of the 2DEG in SrTiO$_3$. The dashed blue circles are guides to the eye for the two Fermi surfaces generated by the light parabolic subbands. (**c**) Spin-resolved populations of spin up and spin down electrons (with respect to $\vec{Q}$) around the Fermi level, as a function of electron momentum along (010). SARPES data was measured within the Gaussian resolution-broadened energy range indicated by the dashed rectangle in (e). (**d**) Resulting angle-resolved spin polarization around E_F along the local spin quantization axis Q. (**e**) Energy-momentum intensity map along (010), violet dashed arrow in (b), showing the two light subbands. The dashed rectangle and bold line in this and other figures indicate the Gaussian energy broadening and energy setting for the SARPES measurements. The black curve on top of the color plot is the ARPES momentum distribution curve (MDC) integrated over the dashed rectangle. (**f**–**h**) Same as (c–e) along the orthogonal momentum direction (100), green dashed arrow in (b). Note from (a) that the angular movements θ and ψ are not equivalent with respect to the scattering plane, causing differences in the shape of the spin polarizations along (100) and (010). All data in this figure was measured at $T = 20$ K using linear-vertical photons at $h\nu = 47$ eV, around angles $\theta = 60°$ and $\psi = 0$ as depicted in panel (a), corresponding to the Γ_{102} Brillouin zone.

FIG. 2. **Spin components at different subband binding energies.** (**a**) Energy-momentum intensity map along (010) (colour plot), and MDC of the total spin-integrated signal (blue circles) recorded by the Mott detectors over the resolution-broadened energy range indicated by the dashed rectangle. (**b**–**d**) Corresponding angle-resolved spin polarizations (black circles) along respectively the local x (tangential to the Fermi surface), y (radial) and z (out-of-plane) axes. The red and blue curves in (a) are Voigt fits for the spin up and spin down populations fitting simultaneously (orange curves) the total spin signal and the spin polarizations along x, y and z. (**e**) Projection on the xy-plane of the resulting 3D spin vectors around E_F. The circles represent the two Fermi surfaces of the light subbands. Arrows represent the measured polarization amplitude of pairs of opposite spin vectors around E_F, obtained from the fits to the spin signal with $|P_{fit}| = 1$. (**f**–**j**) Same as (a–e) at an energy $E_F - 130$ meV, green dashed line in panel (f). Note the decrease of measured polarization amplitude for the spins winding around the inner subband. (**k**–**o**) Same as (a–e) at $E_F - 190$ meV purple dashed line in panel (k). The measured polarization amplitude of the spins in the outer subband drops to 80% of its value around E_F. All data in this figure was measured at $h\nu = 47$ eV on the Γ_{102} Brillouin zone using linear-vertical photon polarization, at a temperature of 20 K.

FIG. 3. **Summary of spin-splittings and spin vectors of the light subbands at the surface of SrTiO$_3$.** (**a**) Schematic representation of the spin-split light subbands at the surface of SrTiO$_3$, assigning a number to each of the subband branches. The two subbands are separated by an energy gap of about 100 meV for all momenta from $\vec{k} = 0$ to k_F. Each subband is spin polarized, with spins winding in opposite directions for opposite momenta at a given binding energy. This is depicted by the arrows and the red and blue hues in different subband branches. For each band, the measured in-plane spin polarization decreases as one approaches the bottom of the band, and is schematically represented by the width of the parabolae. (**b**) Definition of the local $\{xyz\}$ axes and polar representation of the 3D spin vectors (red ball-pointed arrows) used in the remaining plots of this figure. (**c**–**f**) 3D spin vectors at E_F for each of the subband branches (1 to 4), obtained from 4 different sets of measurements at respectively $h\nu = 52$ eV using linear-vertical (LV) photons, and at $h\nu = 47$ eV using circular left-handed (C$^-$), circular right-handed (C$^+$), and LV photons. All data presented in this figure was measured on the Γ_{102} Brillouin zone at 20K.
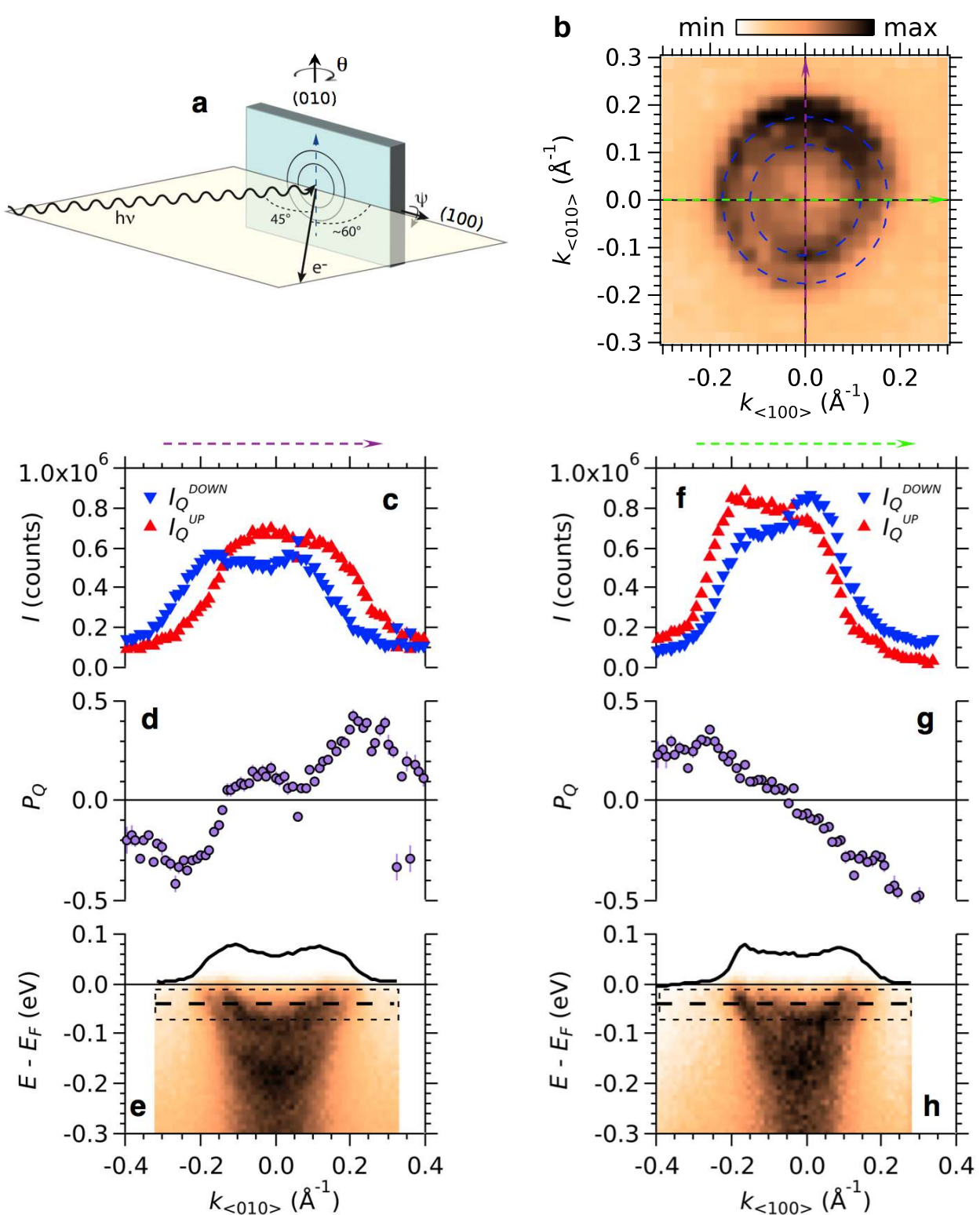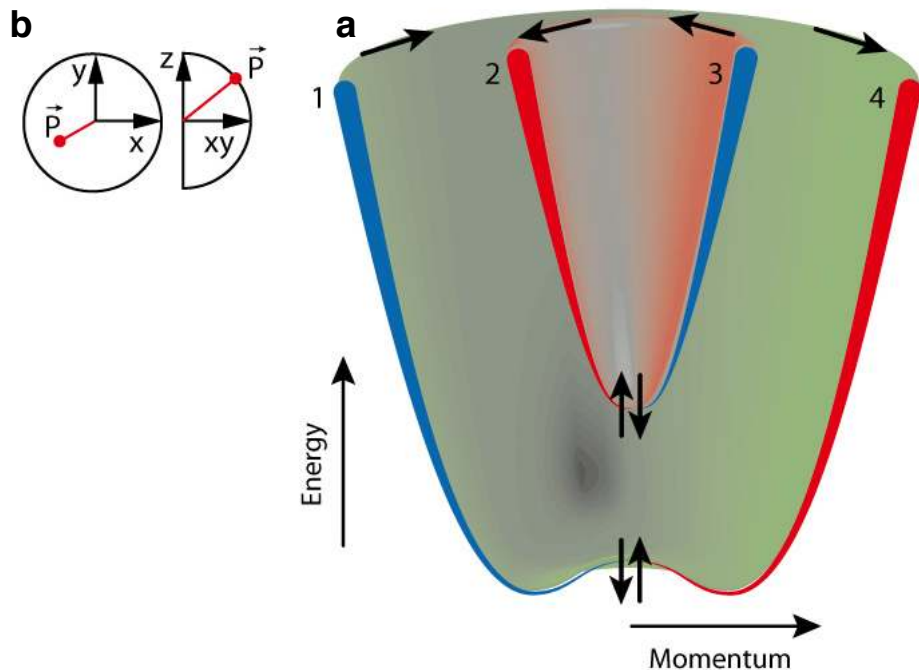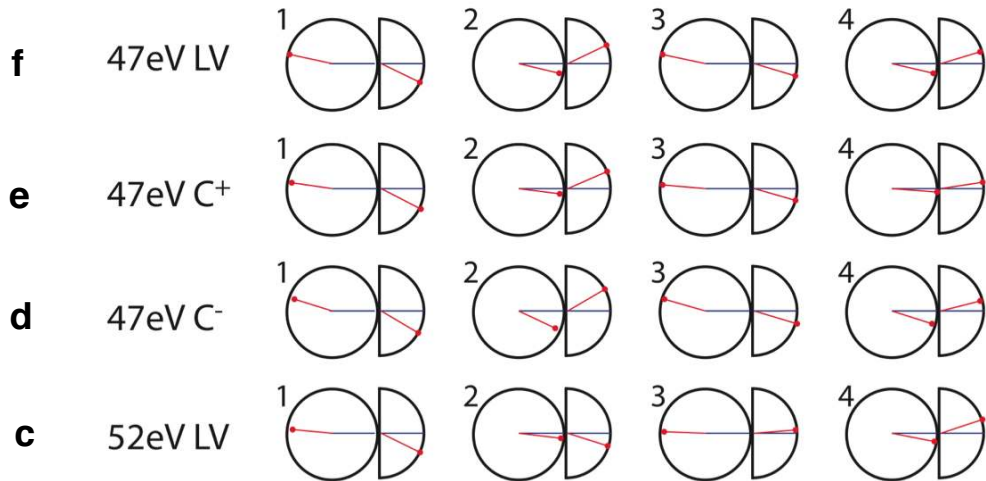
Figure 1. A. F. Santander-Syro, F. Fortuna, C. Bareille, T. C. Rödel, G. Langdolt, N. C. Plumb, J. H. Dil, and M. Radovic
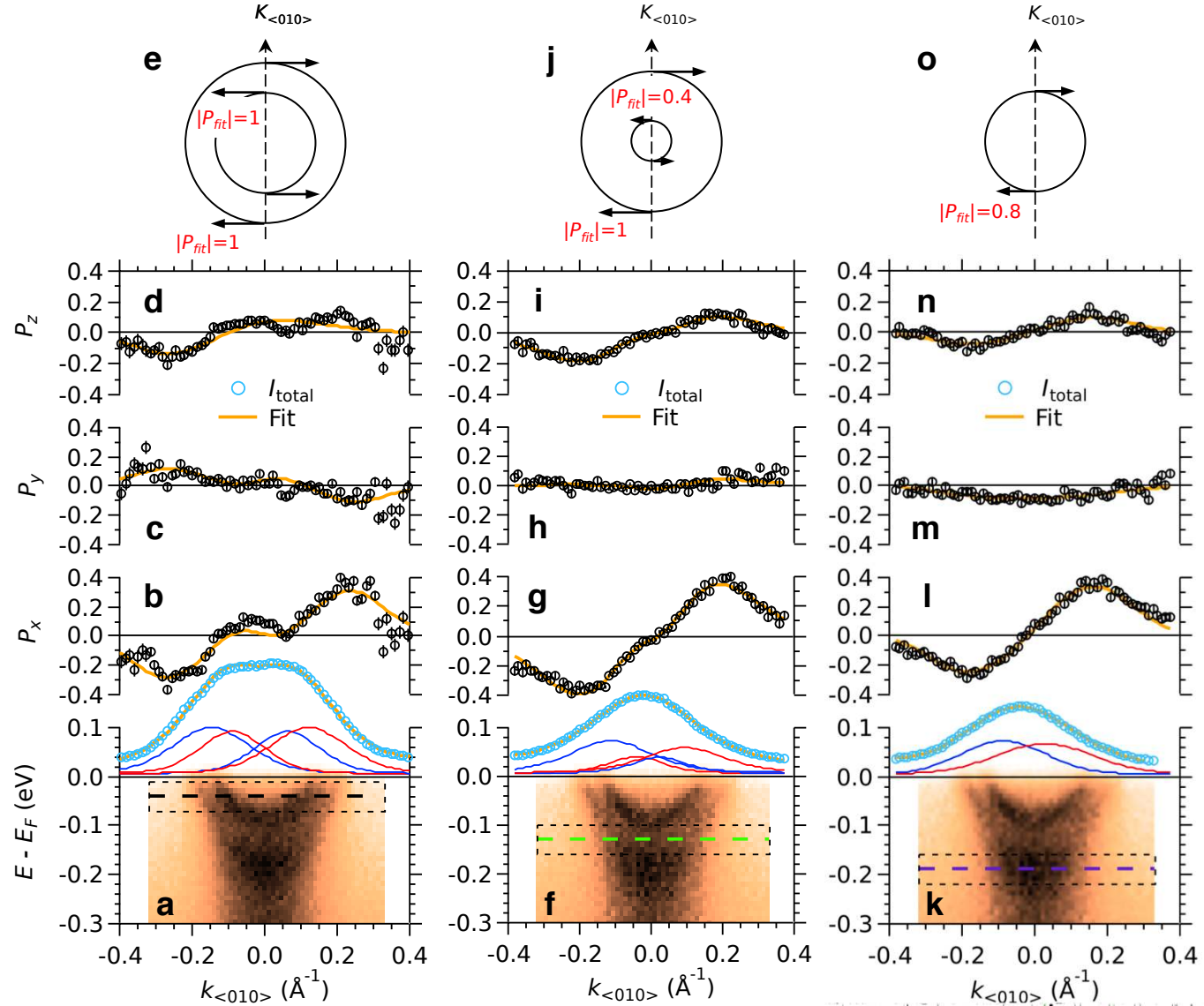
Figure 2. A. F. Santander-Syro, F. Fortuna, C. Bareille, T. C. Rödel, G. Langdolt, N. C. Plumb, J. H. Dil, and M. Radovic

Figure 3. A. F. Santander-Syro, F. Fortuna, C. Bareille, T. C. Rödel, G. Langdolt, N. C. Plumb, J. H. Dil, and M. Radovic

SUPPLEMENTARY MATERIAL

Giant spin splitting of the two-dimensional electron gas at the surface of SrTiO$_3$

A. F. Santander-Syro,[1, *] F. Fortuna,[1] C. Bareille,[1] T. C. Rödel,[1]

G. Landolt,[2, 3] N. C. Plumb,[3] J. H. Dil,[2, 3, 4, †] and M. Radović[3, 5, ‡]

[1]*CSNSM, Université Paris-Sud and CNRS/IN2P3,*

Bâtiments 104 et 108, 91405 Orsay cedex, France

[2]*Physik-Institut, Universität Zürich,*

Winterthurerstrasse 190, 8057 Zürich, Switzerland

[3]*Swiss Light Source, Paul Scherrer Institut, CH-5232 Villigen PSI, Switzerland*

[4]*Institute of Condensed Matter Physics,*

Ecole Polytechnique Fédérale de Lausanne, CH-1015 Lausanne, Switzerland

[5]*SwissFEL, Paul Scherrer Institut, CH-5232 Villigen PSI, Switzerland*

Supplementary Note 1: 2DEG on SrTiO$_3$ prepared *in situ*: light and heavy subbands.

For our experiments, we prepared *in situ* the 2DEG on (001)-oriented TiO$_2$ terminated surfaces, as described in the Methods section of the main text. The 2DEG so obtained shows light and heavy subbands *identical* to the ones observed in cleaved SrTiO$_3$ surfaces [SR1, SR2], but with much sharper photoemission lines and a larger signal-to-background ratio. This is crucial, as SARPES measurements have an intrinsically low detection efficiency, implying that the energy and momentum resolutions need to be degraded to have a good signal-to-noise ratio.

Figures S1(a, b) show spin-integrated energy-momentum intensity maps along (010) (color plots) recorded by the SARPES channeltron at $h\nu = 85$ eV (Brillouin zone Γ_{003}) on the same spot of the sample. Using linear vertical (LV) photon polarization, Fig. S1(a), one observes only the light subbands, while using linear horizontal (LH) polarization, Fig. S1(b), one detects a heavy subband and a very weak signal from the outer light subband. These changes are due to dipole-transition selection rules and the different orbital characters of the light and heavy subbands of the 2DEG at the surface of SrTiO$_3$ [SR1].

As stated in the main text, we focus in this work only on the two light subbands, and silence the the heavy subband by taking advantage of selection rules in the Γ_{102} Brillouin zone, as thoroughly discussed in Ref. [SR1].

Supplementary Note 2: Projection of the raw polarization data on the quantization axis $\vec{Q}$.

In Fig. 1 of the main text, the SARPES data is presented projected on the *local* quantization axis. This is so because for systems with strong spin-orbit interaction, unlike purely ferromagnetic systems, the quantization axis $\vec{Q}$ can be a function of the electron momentum $\vec{k}$: $\vec{Q} = \vec{Q}(\vec{k})$. Therefore, a simple method is required to plot the data along this a-priori unknown quantization axis. This method should be independent of any assumptions or fitting parameters, and should provide an easy way to present the data in an intuitive spin-up/spin-down fashion.

The magnitude of the polarization along the quantization axis can be easily obtained

using Pythagoras theorem:

$$|P_Q| = \sqrt{P_x^2 + P_y^2 + P_z^2},$$

where P_x, P_y and P_z are the spin polarizations along the local x (tangential to the Fermi surface), y (radial) and z (out-of-plane) axes. A caveat is that, in this case, the sign of the spin polarization along $\vec{Q}$ is lost. However, as shown in figures 2 and 3 of the main text, and in the raw spin-polarized intensities along the local $\{xyz\}$ axes, presented in Fig. S2, the main polarization component is along the x direction. Thus, the local x axis is the closest to the local quantization axis, and we choose to take the sign of this component as the sign of P_Q. This yields:

$$P_Q = \frac{P_x}{|P_x|} \times \sqrt{P_x^2 + P_y^2 + P_z^2}$$

This choice of the sign results in the three data points with the correct amplitude but wrong sign in Fig. 1(d) of the main text, because there the x-polarization has a zero crossing, as visible in Fig. 2(b) of the main text or Fig. S2(b).

It should be noted that although this method projects the data on the quantization axis, the direction of this axis remains unknown and a fitting procedure, such as in Fig. 2 of the main text, is required to determine it.

Supplementary Note 3: Measurements of the spin polarizations at E_F for different photon energies and light polarizations.

All data presented in the main text was measured at $h\nu = 47$ eV on the Γ_{102} Brillouin zone using LV photon polarization. Figure S3 presents three further sets of data showing the spin polarizations at E_F measured with, respectively, circular right-handed (C^+) polarization at $h\nu = 47$ eV [panels (a–d)], circular left-handed (C^-) polarization at $h\nu = 47$ eV [panels (e–h)], and LV polarization at $h\nu = 52$ eV [panels (i–l)].

The different sets of measurements in Fig. S3 are compatible with each other, and consistently reproduce the data discussed in the main text. As noted in the main text, the sole anomaly is the inverted out-of-plane (z) component of the spin polarization at $h\nu = 52$ eV, that we observe only at this photon energy. Given that along this crystal orientation an intrinsic out-of-plane spin component is not allowed, due to symmetry considerations, we attribute the observed component to a matrix element of the SARPES process [SR3]. We

stress that, contrary to the anomalous behavior of P_z, P_x is wholly compatible between all the data sets, which strongly indicates that this latter component of the spin polarization is intrinsic.

Supplementary Note 4: Simulation of the combined effects of intrinsic Rashba and Zeeman splittings.

As stressed in the main part of our work, the shape of Fig. 3(a) is an oversimplification, whose sole purpose is to indicate that our results can be assimilated to two Rashba parabolae further split by an intrinsic magnetic moment at $\vec{k} = 0$. However, we are not advocating in this work for a specific model to describe our data. Keeping that in mind, we show here that a simplified model of intrinsic Rashba plus Zeeman splittings can indeed reproduce reasonably well the observed band dispersions and in-plane spin polarizations.

In fact, from the essentially parabolic shape of the light bands at the surface of SrTiO$_3$, one might feel that the only possibility is to have a very small Rashba splitting, of a few meV (as the one reported in LaAlO$_3$/SrTiO$_3$ heterostructures [SR4]), and a large intrinsic Zeeman splitting of about 100 meV (the splitting at $\vec{k} = 0$). However, as we will see next, the observation of *both* a large spin-splitting at E_F *and* a large in-plane spin polarization for several momenta (near E_F and at lower binding energies) implies that the Rashba splitting is comparable or larger than the intrinsic Zeeman field.

We assume a simplified phenomenological description using parabolic bands (effective mass $m^\star$), spin-split by a k-linear Rashba term (coupling constant α) plus a momentum-independent internal Zeeman field (full gap at $\vec{k} = 0$ equal to Δ_Z). The Hamiltonian of this model is:

$$H - E_0 = \frac{p^2}{2m^\star} + \frac{\Delta_Z}{2}\sigma_z + \frac{\alpha}{\hbar}(p_x \times \sigma_y - p_y \times \sigma_x), \tag{1}$$

where E_0 is the band bottom and σ_i $(i = x, y, z)$ are the Pauli matrices. The energies of the spin-split states along the measured momentum direction k are then:

$$E_\pm(k) = E_0 + \frac{\hbar^2 k^2}{2m^\star} \pm \frac{1}{2}\sqrt{\Delta_Z^2 + 4\alpha^2 k^2}. \tag{2}$$

From the Hamiltonian above, one can also calculate the momentum-dependent expected values of the spin components ($< S_x >$, $< S_y >$ and $< S_z >$) for the two eigenstates associated to the above eigenenergies. We omit here for brevity the straightforward calculation.

4

Thus, to describe the data using the above model, we fit simultaneously the observed band dispersions and the measured in-plane spin polarizations for each momentum. This restrains to a very narrow range the possible values of the Rashba coupling constant and the Zeeman splitting.

As shown in Fig. S4, the best fit is obtained using an effective mass $m^\star = 0.65 m_e$ (similar to previous reports [SR1, SR2, SR5]), a Zeeman splitting $\Delta_Z = 80$ meV, which differs by 11% of the experimental value of 90 meV, and a Rashba coupling constant $\alpha = 5 \times 10^{-11}$ eV m, which is 10 times larger than what is commonly quoted in the theoretical or experimental literature for $LaAlO_3/SrTiO_3$ heterostructures, namely $\alpha_{max} = 5 \times 10^{-12}$ eV m [SR4], and which produces (in the absence of a Zeeman field) a Rashba spin splitting at the Fermi level of 120 meV, larger than the Zeeman field, and again more than 10 times larger than the maximum values quoted in the theoretical literature for the Rashba energy splitting in $LaAlO_3/SrTiO_3$. We checked that reducing the Rashba coupling constant by more than 15% does not give anymore an acceptable fit of both the dispersions and the in-plane spin amplitudes.

Hence, the spin-integrated data alone is in fact compatible with Rashba splittings that can be of the same order of magnitude or even larger than the splitting at $\vec{k} = 0$. As emphasized in the main text, each subband maintains a non-trivial spin-texture with large in-plane spin polarization down to the lowest binding energies, suggesting that, besides the Zeeman splitting, the helical spin splitting, whatever its origin, is larger than what may be expected in a simple Rasha scenario.

––––––––––

* andres.santander@csnsm.in2p3.fr

† hugo.dil@epfl.ch

‡ milan.radovic@psi.ch

[SR1] Santander-Syro, A. F., Copie, O., Kondo, T., Fortuna, F., Pailhès, S., Weht, R., Qiu, X. G, Bertran, F., Nicolaou, A., Taleb-Ibrahimi, A., Le Fèvre, P., Herranz, G., Bibes, M., Reyren, N., Apertet, Y., Lecoeur, P., Barthélémy, A., and Rozenberg, M. J. Two-dimensional electron gas with universal subbands at the surface of $SrTiO_3$. *Nature* **469,** 189-193 (2011).

[SR2] Plumb, N. C., Salluzzo, M., Razzoli, E., Månsson, M., Falub, M., Krempasky, J., Matt, C.

E., Chang, J., Schulte, M., Braun, J., Ebert, H., Minár, J., Delley, B., Zhou, K.-J., Schmitt, T., Shi, M., Mesot, J., Patthey, L., and Radović, M. Mixed dimensionality of confined conducting electrons in the surface region of SrTiO$_3$. *Phys. Rev. Lett.* **113,** 086801 (2014).

[SR3] Mirhosseini, H., Flieger, M., and Henk, J. Dirac-cone-like surface state in W(110): dispersion, spin texture and photoemission from first principles. *New J. Phys.* **15,** 033019 (2013).

[SR4] Caviglia, A. D., Gabay, M., Gariglio, S., Reyren, N., Cancellieri, C., and Triscone, J.-M. Tunable Rashba spin-orbit interaction at oxide interfaces. *Phys. Rev. Lett.* **104,** 126803 (2010).

[SR5] Meevasana, W., King, P. D. C., He, R. H., Mo, S.-K, Hashimoto, M., Tamai, A., Songsiriritthigul, P., Baumberger, F., and Shen, Z.-X. Creation and control of a two-dimensional electron liquid at the bare SrTiO$_3$ surface. *Nature Mater.* **10,** 114-118 (2011).
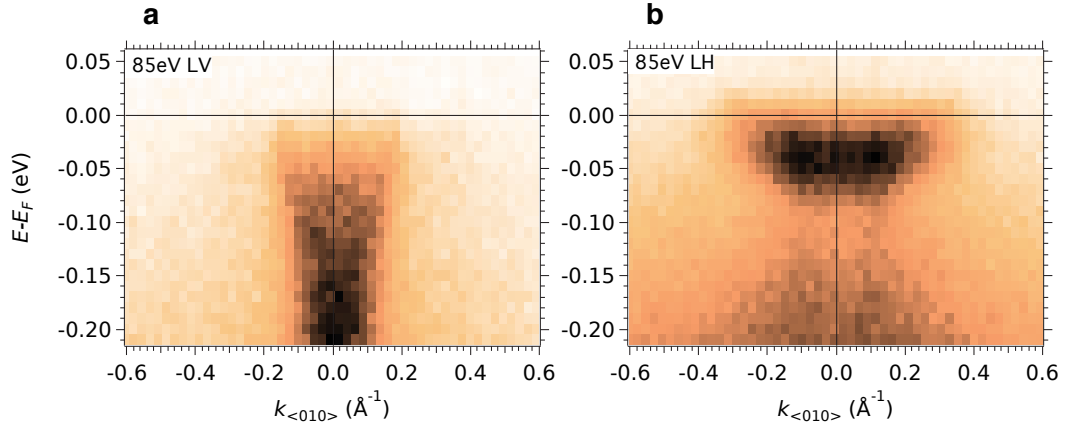
Figure S 1. **Light and heavy subbands at the surface of SrTiO$_3$ detected by the COPHEE channeltrons.** (**a**) Energy-momentum intensity maps along (010) recorded by the SARPES channeltron at $h\nu = 85$ eV (Brillouin zone Γ_{003}) using LV photon polarization. (**b**) Same as (a) using LH polarization. All data were measured at $T = 20$K.
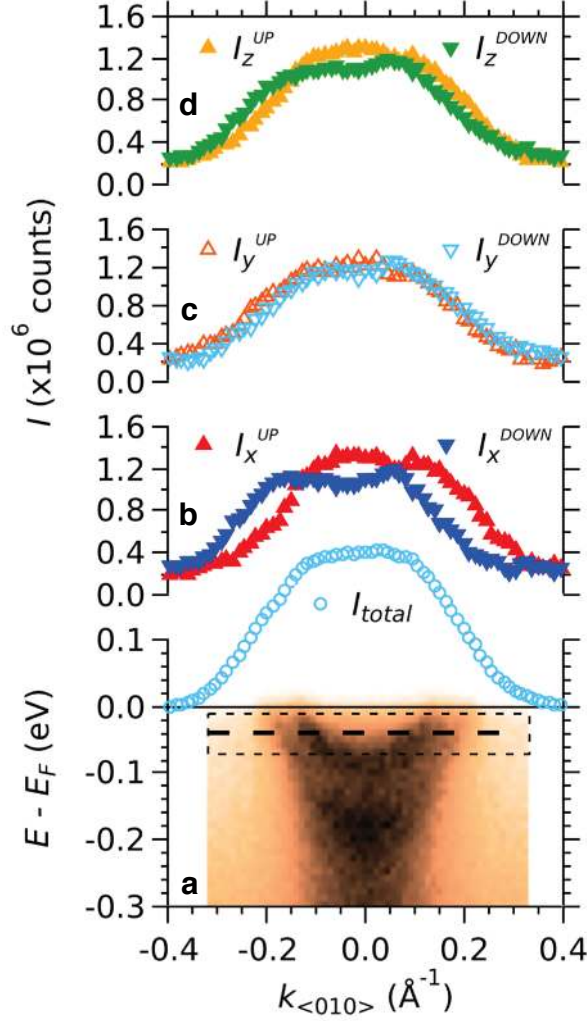
Figure S 2. **Raw spin-polarized intensities along the local $\{xyz\}$ axes.** (**a**) Energy-momentum intensity map along (010), showing the two light subbands, and corresponding MDC (blue circles) of the total spin-integrated signal recorded by the Mott detectors within the resolution-broadened energy range near E_F indicated by the dashed rectangle. (**b**) Spin-resolved populations of spin up and spin down electrons (with respect to the local x axis) at the Fermi level as a function of electron momentum along (010). Note the clearly-resolved separation between the spin up and spin down populations, corresponding to the momentum separation between the two light subbands. (**c**–**d**) Same as (**b**) along the local y and z axes, respectively. In both cases, the separation between spin up and spin down populations is much smaller than along x. Hence, the local quantization axis at E_F is quasi-tangential to the Fermi surfaces. All data presented in this figure was measured at $h\nu = 47$ eV on the Γ_{102} Brillouin zone using linear-vertical photon polarization at $T = 20$K.
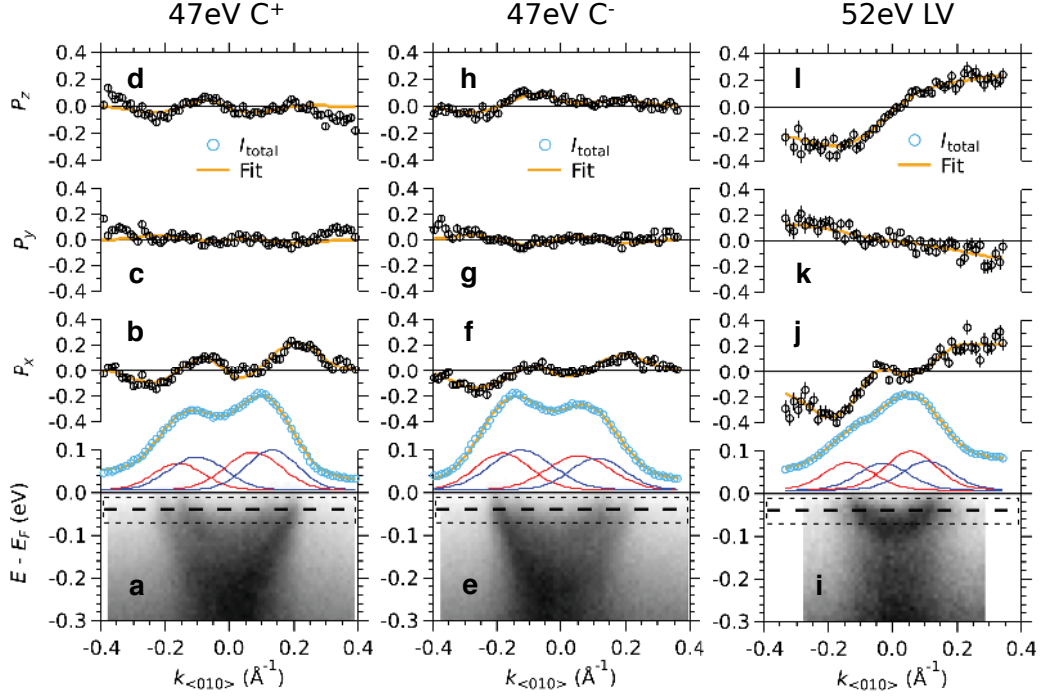
8

Figure S 3. **Spin polarized subbands at the surface of SrTiO$_3$ for different photon polarizations and energies.** (**a–d**) SARPES data measured at $h\nu = 47$ eV on the Γ_{102} Brillouin zone using circular right-handed photon polarization. Panel (a) shows the energy-momentum intensity map along (010) (colour plot) and the MDC (blue circles) of the total spin-integrated signal recorded by the Mott detectors within the resolution-broadened energy range near E_F indicated by the dashed rectangle. Panels (b–d) show the angle-resolved spin polarizations near E_F (black circles) along respectively the local x (tangential to the Fermi surface), y (radial) and z (out-of-plane) axes. The red and blue curves in panel (a) are Voigt fits for the spin up and spin down populations fitting simultaneously (orange curves) the total spin signal and the spin polarizations along x, y and z. (**e–h**) Same as (a–d) using circular left-handed photon polarization. (**i–l**) Same as (a–d) measured at $h\nu = 52$ eV on the Γ_{102} Brillouin zone using linear-vertical photon polarization. All data in this figure were measured at $T = 20$K.
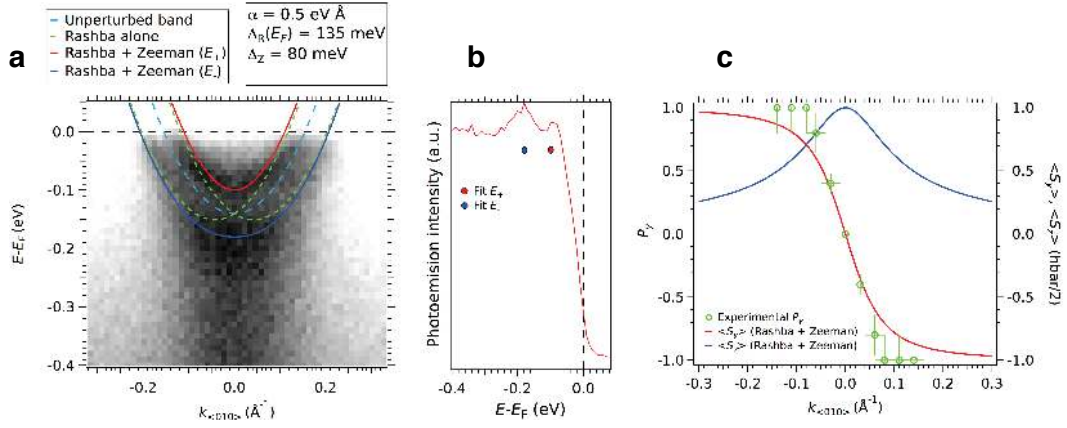
9

Figure S 4. **Simplified simulation of the combined effects of intrinsic Rashba and Zeeman splittings.** (**a**) Experimental energy-momentum intensity map along (010) (colour plot) and fits using a simplified parabolic-band model subject to both Rashba and Zeeman splittings, with the intrinsic Zeeman field along (001). The dashed light-blue parabola is the unperturbed spin-degenerate band. The dotted green parabolas are the states resulting from a Rashba splitting of 135 meV at the Fermi level, using a Rashba coupling constant of $\alpha = 5 \times 10^{-11}$ eV m. The solid blue and red lines are the same states, further split by a Zeeman field of 80 meV. (**b**) Energy distribution curve at $\vec{k} = 0$, obtained by integrating the intensity map in (a) over the interval $k_{<010>} = [-0.5, 0.5]$ Å^{-1}. The peaks of the upper and lower subbands are clearly visible, and are separated by an energy gap of 90 meV. The filled red and blue circles show the band bottoms of the fits in panel (a). (**c**) Experimental in-plane spin polarizations for different momenta (green circles) and expected values of the tangential ($< S_y >$) and out-of-plane ($< S_z >$) polarization (red and blue lines) given by the same parameters used to fit the bands in panel (a). The experimental points were extracted from the data presented in figure 2 of the main text. The vertical bars represent an error of 20% in the determination of the in-plane polarization.